

DEPENDENCY OF PHOTO-Z ACCURACY ON FILTER DEFINITION OF PHOTOMETRIC SURVEYS

YE CAO^{1,2}, YAN GONG^{1†}, XIAN-MIN MENG³, CONG K. XU^{4,5}, XUELEI CHEN^{1,2,6}, QI GUO¹,
 RAN LI^{1,2}, DEZI LIU⁷, YONGQUAN XUE^{8,9}, LI CAO³, XIYANG FU³, XIN ZHANG³, SHEN WANG³, HU ZHAN³

¹ Key Laboratory for Computational Astrophysics, National Astronomical Observatories,
 Chinese Academy of Sciences, 20A Datun Road, Beijing 100012, China

² School of Astronomy and Space Sciences, University of Chinese Academy of Sciences, Beijing 100049, China

³ Key Laboratory of Space Astronomy and Technology, National Astronomical Observatories,
 Chinese Academy of Sciences, Beijing 100012, China

⁴ National Astronomical Observatories, Chinese Academy of Sciences, 20A Datun Road, Beijing 100012, China
⁵ South American Center for Astronomy, CAS, Camino El Observatorio 1515, Las Condes, Santiago, Chile

⁶ Center for High Energy Physics, Peking University, Beijing 100871, China

⁷ Department of Astronomy, School of Physics, Peking University, Beijing 100871, China

⁸ CAS Key Laboratory for Research in Galaxies and Cosmology, Department of Astronomy,
 University of Science and Technology of China, Hefei 230026, China and

⁹ School of Astronomy and Space Science, University of Science and Technology of China, Hefei 230026, China

Draft version December 14, 2024

ABSTRACT

Accurate measurement of photometric redshift (photo- z) is crucial for photometric galaxy surveys, hence it is very important to study how the photo- z accuracy depends on the design of filter systems, and find the best filter parameters which can optimize photo- z fitting. Here we investigate this problem for the Chinese Space Station Optical Survey (CSS-OS) as an example, which covers wide wavelength range from near-ultraviolet to near-infrared bands. We use the COSMOS galaxy catalog to create mock flux data, whose galaxy redshift and magnitude distributions are similar to that of the CSS-OS. We compared different public photo- z spectral energy distribution (SED) template-fitting codes, and choose to use a modified LePhare code in the filter calibration process. The code exploits information in flux upper-limits, which has been proven to be effective in the photo- z measurement. We then investigate the effect of each filter passband and filter parameters on photo- z fitting. We find that the g , r , and i bands can significantly affect the photo- z accuracy and fraction of catastrophic redshift in the CSS-OS or any survey with similar magnitude limits, and the current CSS-OS filter design can optimize the photo- z fitting process.

Subject headings: cosmology: observations - theory - large-scale structure of universe

1. INTRODUCTION

Photometric sky survey is a basic observation for modern astronomy research. The positions of large number of targets on the celestial sphere and their fluxes in several wavelength bands defined by photometric filters are obtained by such surveys. A number of ongoing and planned large photometric surveys with large areas and deep fields are well known, e.g. the Sloan Digital Sky Survey (SDSS)¹, the Large Synoptic Survey Telescope (LSST) (Abell et al. 2009), the Euclid space telescope (Laureijs et al. 2011), etc. These surveys can provide us much information on the distribution of galaxies. The large scale structure distribution of galaxies is one of the primary source of data for modern cosmology, which is very valuable in solving a number of fundamental problems, such as the properties of dark energy and dark matter, the origin of the Universe, and formation and evolution of galaxies. However, high precision measurements of the three dimensional positions of galaxies require spectroscopic redshift measurements, but spectroscopic surveys are always much slower than photometric surveys. Nevertheless, an estimate of the redshift can be obtained from the photometric survey. Although not as precise as the spectroscopic redshift, in a number of important applications (e.g. lensing tomography) the photo-

tometric redshift (photo- z) is adequate for current studies. Furthermore, it is also very useful when selecting a sub-sample of targets for a spectroscopic survey. Thus, it is very important to understand how the photo- z accuracy varies as the parameters of the photometric filters change, so that one can design a good set of photometric filter system for the survey to improve photo- z calibration.

Many methods for estimating redshift from the photometric data have been developed over the years, roughly speaking, they can be classified as two types. One type may be called “template fitting” method, which extracts redshift by fitting photometric data with the templates of galaxy spectral energy distributions (SEDs). Publicly available codes of this type include Hyperz (Bolzonella et al. 2000), BPZ (Benitez 2000), ZEBRA (Feldmann et al. 2006), EAZY (Brammer et al. 2008), LePhare (Arnouts et al. 1999; Ilbert et al. 2006), etc. Another type may be called “training set” method, which obtains an empirical relation between redshift and galaxy properties (e.g. magnitude and color) using a galaxy sample with measured spectroscopic redshifts. The neural network code ANNz (Firth et al. 2003; Collister & Lahav 2004) is of this type. These two approaches have different advantages, we would adopt the SED fitting technique in this study, since it is more flexible and suitable for our discussion.

In this work, we take the imaging part of the Chinese

E-mail: gongyan@bao.ac.cn

¹ <http://www.sdss.org/>

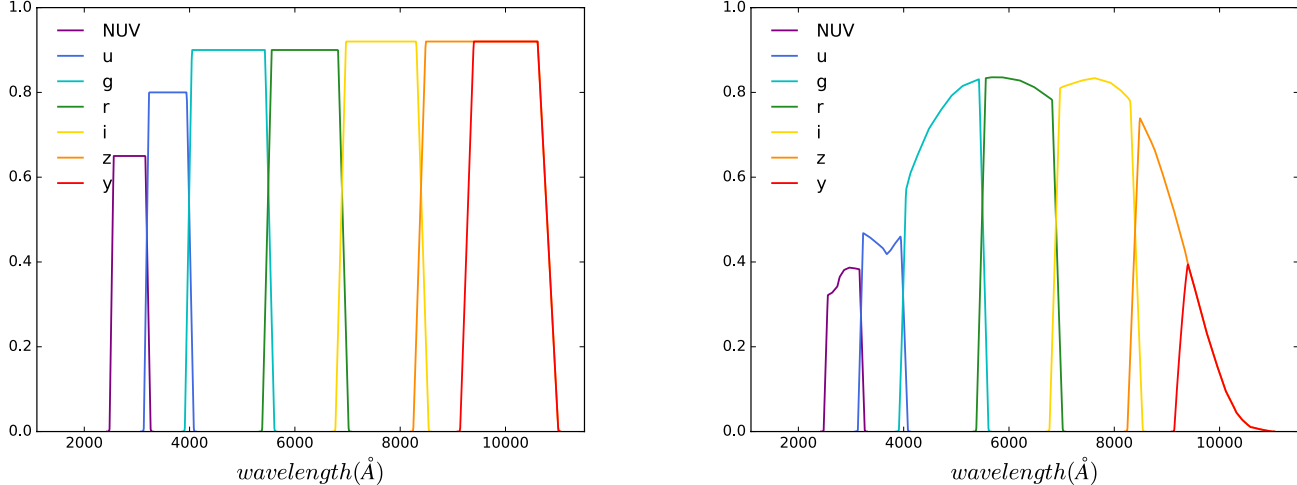


FIG. 1.— *Left* : The intrinsic transmission curves for the seven filters from NUV to NIR bands, including the *NUV*, *u*, *g*, *r*, *i*, *z*, and *y* bands. *Right* : The total transmission by considering detector quantum efficiency.

Space Station Optical Survey (CSS-OS) as the example for our discussion. As part of the Chinese Space Station science program, this survey shall have large field of view, high spatial resolution, faint magnitude limits, and wide wavelength coverage from near-ultraviolet (NUV) to near infrared (NIR) bands (Zhan 2011). It would be the basis for many kinds of cosmological and astronomical observations, including weak lensing, baryon acoustic oscillation (BAO), galaxies and galaxy clusters, active galactic nuclei (AGN), etc. Based on these observations, fundamental questions about gravity, dark matter and dark energy, the large scale structure of our Universe, galaxy formation and evolution, the formation of super-massive black hole and so on could be investigated. All of these scientific goals are heavily dependent on the accuracy of the photometric redshifts.

In order to simulate the observational data as real as possible, we make use of the COSMOS galaxy catalog (Ilbert et al. 2009), whose magnitude limit is similar to the nominal value of the CSS-OS, and therefore also has similar galaxy redshift distribution, magnitude distribution, and galaxy types, though the CSS-OS would cover much wider sky area. Using this catalog, we select sub-sample with high data quality, generate mock flux data for each filter passband, and estimate the observational errors. After comparing different photo-*z* fitting codes, we choose to use a modified LePhare code to perform the filter calibration. The code improves upon LePhare by including information in flux upper-limits. We find this can substantially suppress the fraction of catastrophic redshift and improve the fitting accuracy. Then we discuss the effect of each band on photo-*z* accuracy by omitting these bands, and then checking the variance and catastrophic redshift fraction of photo-*z* fitting results. We also investigate dependency of photo-*z* accuracy on different parameters of the filter transmission curve, such as the position of central wavelength of each band, the wavelength width, and the slope of transmission curve. According to these discussions, we try to find the best design for the filters of photometric survey that can obtain the most accurate photo-*z* measurements.

This paper is organized as follows: in Section 2, we in-

TABLE 1
THE CSS-OS FILTER DEFINITION.

Filter	λ_{mean} (Å)	FWHM (Å)	λ_{lb} (Å)	λ_{lt} (Å)	λ_{rt} (Å)	λ_{rb} (Å)	Trans.
<i>NUV</i>	2877	701	2480	2550	3260	3170	65%
<i>u</i>	3595	847	3130	3220	3960	4080	80%
<i>g</i>	4798	1562	3910	4030	5450	5610	90%
<i>r</i>	6186	1471	5380	5540	6840	7020	90%
<i>i</i>	7642	1577	6770	6950	8330	8540	92%
<i>z</i>	9046	2477	8250	8460	10650	11000	92%
<i>y</i>	9654	1576	9140	9370	10650	11000	92%

roduce the filter definition of CSS-OS, and the method used to create the mock data. In Section 3, we explore three currently widely-used photo-*z* fitting codes, i.e. LePhare, EAZY and Hyperz, and compare their fitting results. In Section 4, we investigate the dependency of photo-*z* accuracy on the filters and design parameters of the CSS-OS. We finally summarize the results in Section 5.

2. MOCK GALAXY FLUX DATA

In this section, we first introduce the CSS-OS filter definition, then discuss the galaxy catalog we use to simulate the CSS-OS observations, and finally give the estimations of flux and error from galaxy SED models.

2.1. The CSS-OS filter definition

Based on current telescope instrument design, the CSS-OS will be conducted with a combination of 7 broad-band filters, and their nominal AB magnitude 5σ limits are $NUV \simeq 25.4$, $u \simeq 25.5$, $g \simeq 26.2$, $r \simeq 26.0$, $i \simeq 25.8$, $z \simeq 25.7$ and $y \simeq 25.5$ for point sources. In Figure 1, we show the transmission curves for seven filters that are under test. The left panel shows the intrinsic transmission curves, and the right panel gives the total transmission including the detector quantum efficiency. The definition parameters for the filters are listed in Table 1. Here we show the mean wavelength λ_{mean} , full width at half maximum (FWHM), and the wavelength region of the top and bottom transmission curve from left to right (i.e. λ_{lt} and λ_{rt} , and λ_{lb} and λ_{rb}). The top transmission efficiency for

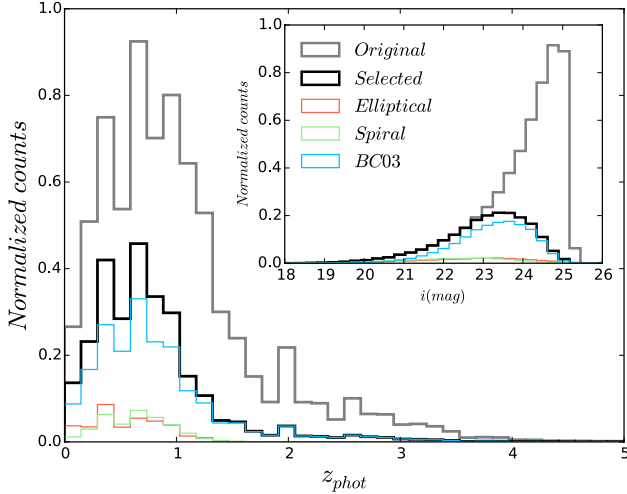


FIG. 2.— The redshift and magnitude distributions of the COSMOS galaxy catalog we use (Ilbert et al. 2009). The gray and black histograms show the original and high-quality selected galaxy samples, respectively. The distributions of elliptical, spiral, and young blue star forming (fitted by the BC03 method, and labeled as BC03 following Ilbert et al. (2009)) galaxies of the selected sample are also shown in red, green and blue histogram, respectively.

each band is estimated to be 65% for NUV , 80% for u , 90% for g and r bands, and 92% for i , z and y bands, respectively. This filter definition is the basic case which is used in our following discussion, and we will study how to optimize it for improving photo- z accuracy with the galaxy catalog we adopt as described below.

2.2. Galaxy Catalog

In order to study the photo- z calibration for the CSS-OS, we first need to find a galaxy catalog which can represent our survey, and has similar redshift and magnitude distributions as expected for ours. Since the magnitude limit of the CSS-OS can achieve $i \sim 26$ for point source with 5σ detection, it is expected to be about one or two magnitudes brighter for galaxy surface sources. Here we make use of the COSMOS galaxy catalog from an accurate photo- z survey in 2-deg 2 COSMOS field (Ilbert et al. 2009). This catalog contains about 380,000 objects, which are measured in 30 bands from Subaru Telescope, Canada-France-Hawaii Telescope (CFHT), Spitzer-IRAC, etc. After removing stars, X-ray, masked, and poorly-measured faint sources, we obtain about 219,000 galaxies as our original galaxy catalog. This original catalog includes the necessary information for generating mock data, such as the redshift, magnitude, galaxy type, and galaxy size. In order to perform the photo- z fitting with required accuracy, we also need to select sources with high data quality. Here we calculate the signal to noise ratio (SNR) for each galaxy in the catalog (see Section 2.3 for details of the SNR estimation), and select the sources with $\text{SNR} \geq 10$ in g or i band. Then we get $\sim 80,100$ sources ($\sim 37\%$ of the original galaxy catalog) after the selection². Finally, 10,000 galaxies are randomly selected from the high-quality se-

² We find that about 187,000 galaxies ($\sim 86\%$ of the original sample) can be selected if requiring a typical value of the photo- z fitting variance $\sigma_z \simeq 0.05$ (defined in Section 3).

lected sample, which has similar redshift and magnitude distributions, and will be used in our photo- z calibration.

The redshift and magnitude distributions of the catalogs are shown in Figure 2. We show the original and selected samples in gray and black histograms, respectively. We can see that the redshift distribution of the selected sample has a peak around $z = 0.6$, and can extend to $z \sim 4$. The peak of its magnitude distribution is at $i \sim 23.5$, and the range is from $i \sim 19$ to 25. As compared to the distributions of the original sample, we find that the majority of faint sources with $i \gtrsim 24$ is removed in the selected sample over the whole redshift range. This also indicates that we do not need to adopt galaxy catalogs with higher magnitude limits, e.g. the COSMOS15 catalog (Laigle et al. 2016), since the fainter sources will be discarded by this selection.

The redshift and magnitude distributions of elliptical, spiral, and young blue star forming (fitted by the method given in Bruzual & Charlot (2003), hereafter BC03) galaxies are also shown in red, green and blue histograms, respectively. We find that the percentages of these three kinds of galaxies are 74% for young blue star forming, 13% for spiral, and 13% for elliptical galaxies, which means the young blue star forming galaxies are dominant in the selected catalog. The peak of redshift distributions for both young blue star forming and spiral galaxies is at $z \sim 0.6$, which is the same as the total distribution, while it is around $z = 0.3$ for elliptical galaxy.

2.3. Flux and error estimation

For a given galaxy in the catalog, mocked flux in each band can be calculated by convolving the galaxy redshifted SED with the filter response or transmission function, which is given by

$$F_x^{\text{mock}} = \int S_{\text{model}}(\lambda) T_x(\lambda) d\lambda. \quad (1)$$

Here T_x is the response function for band x , $S_{\text{model}}(\lambda)$ is the galaxy SED derived from SED model (based on the LePhare template that fits best the COSMOS data, with extrapolations and modifications that will be discussed in the following), and $\lambda = \lambda_{\text{res}}(1+z)$ where λ_{res} is the rest-frame wavelength. Then F_x^{mock} is rescaled according to the i band apparent magnitude given by the COSMOS galaxy catalog. Note that there is difference between the i bands used in the COSMOS catalog (F814W is used) and in our survey, and we have converted the i band magnitude from the COSMOS catalog to our own when calculating the observed flux.

In Figure 3, we show the intrinsic SED templates that we used to generate mock flux data. They are based on templates taken from the COSMOS template library (Arnouts et al. 1999; Ilbert et al. 2006), which include seven templates for elliptical galaxy, twelve for spiral galaxies (from S0 to Sdm), and twelve for young blue star forming galaxy (starburst ages from 0.03 to 3 Gyr) (Ilbert et al. 2009). The templates of elliptical and spiral galaxies are derived from the templates in Polletta et al. (2007), and the young blue star forming galaxy templates are generated by the BC03 models.

Since the CSS-OS covers large redshift and wavelength ranges, we extend the wavelength coverage of these templates from $\sim 900 \text{ \AA}$ to $\sim 90 \text{ \AA}$ using the BC03 method.

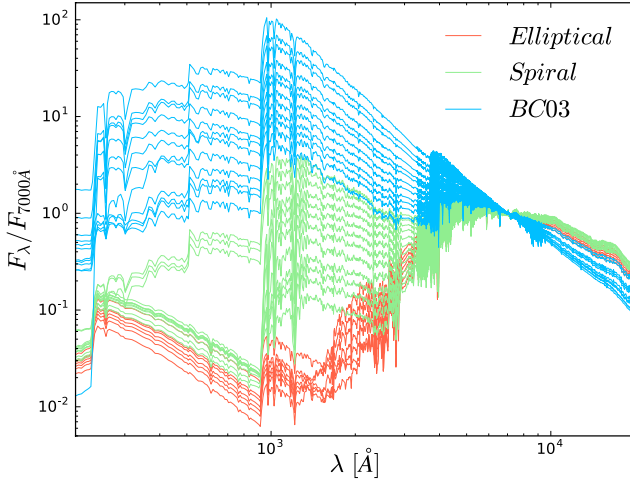


FIG. 3.— The SED templates we use in the analysis. The SEDs of young blue star forming, spiral, and elliptical galaxies, which are derived from the BC03 method and the templates given in Polletta et al. (2007), are shown in blue, green and red curves, respectively. These templates are taken from the COSMOS template library (Arnouts et al. 1999; Ilbert et al. 2006), and we extend them from ~ 900 Å to ~ 90 Å using the BC03 method.

We first fit each SED template with 45 BC03 simple stellar population (SSP) templates in the wavelength range of 915–15000 Å to obtain the stellar components of the SED templates. Then we select 15 ages from 1 Myr to 13 Gyr of BC03 SSPs. The subsolar, solar, and supersolar metallicities of the 15 ages are adopted, and we take $Z = 0.004, 0.02$, and 0.05 for the three cases, respectively. The spectral fitting gives excellent result with reduced $\chi^2 = 0.1 \sim 1.5$. The SED templates can be rebuilt based on the fractions of stellar components and other relevant factors. Finally, the extension of SED templates is achieved by extracting the spectra from the rebuilt SEDs in the wavelength range of 90 Å–160 μm.

The dust extinction effect is also included for the SEDs when generating the mock flux data. The flux density or SED after interstellar dust reddening can be expressed as (Calzetti et al. 1994)

$$S_{\text{ext}}(\lambda_{\text{res}}) = S_{\text{int}}(\lambda_{\text{res}}) 10^{-0.4E(B-V)k(\lambda_{\text{res}})}, \quad (2)$$

where S_{int} is the intrinsic galaxy SED given by Figure 3. $E(B-V) = A_V/R_V$ is the color excess, where A_V follows the probability distribution $P(A_V) \propto e^{4V}/\tau_0$ with $\tau_0 = 0.3$ (Holwerda et al. 2015). $k(\lambda)$ is the dust extinction curve which is shown in Figure 4. We consider six extinction laws here, which are derived from the studies of the Milky Way (MW) (Allen 1976; Seaton 1979), Large Magellanic Cloud (LMC) (Fitzpatrick 1986), Small Magellanic Cloud (SMC) (Prevot et al. 1984; Bouchet et al. 1985), starburst galaxy (SBG) (Calzetti et al. 2000), and star forming galaxy (SFG) (Reddy et al. 2015). The R_V for these laws are 3.1, 3.1, 3.1, 2.72, 4.05, and 2.505, respectively. According to the previous studies (e.g. Bolzonella et al. 2000), these extinction laws are only valid at different redshift ranges, and then we apply the laws derived from the MW and LMC at $z < 2$, SMC at $z < 4$, SFG at $1.4 < z < 2.6$, and SBG at $z < 6$. In the overlapped redshift range where several extinction laws are

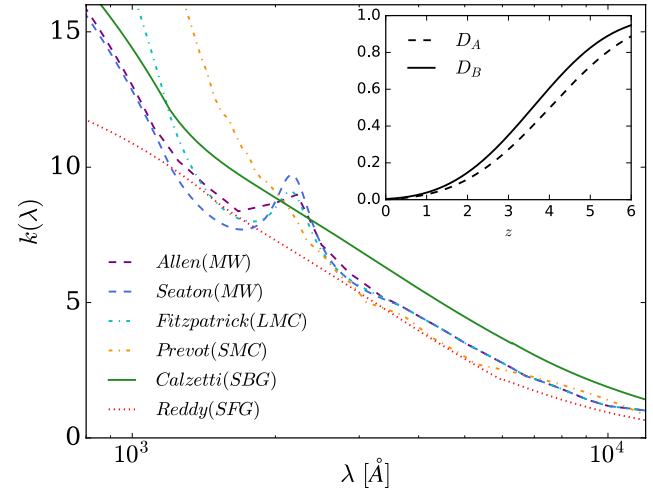


FIG. 4.— The dust extinction laws we adopted in this work. Six extinction laws are shown here, which are obtained from the studies of the Milky Way (MW), Large Magellanic Cloud (LMC), Small Magellanic Cloud (SMC), starburst galaxy (SBG), and star forming galaxy (SFG) (Allen 1976; Seaton 1979; Fitzpatrick 1986; Prevot et al. 1984; Bouchet et al. 1985; Calzetti et al. 2000; Reddy et al. 2015). The absorption by the IGM is also considered, and we use the average flux decrement factors $D_A(z)$ and $D_B(z)$ given by Madau (1995).

available, we randomly select one of them for a galaxy. However, since Calzetti's law from SBG is widely used and available for all redshifts at $z < 6$, we selected it with a higher probability than the other laws by a factor of two.

In addition to the extinction from interstellar dust in galaxies, we also consider the extinction due to absorption of intergalactic medium (IGM) for high- z galaxies. When propagating from high- z galaxies to the observer, the emission at shorter wavelength than the Ly α line can be absorbed by neutral hydrogen clouds in the IGM. In order to include this effect, we make use of the attenuation laws computed by Madau (1995). They give the average flux decrements D_A between Ly α and Ly β , and D_B between Ly β and the Lyman limit, which are defined as

$$D_i \equiv \langle 1 - S_{\text{abs}}/S_{\text{ini}} \rangle, \quad i = A, B. \quad (3)$$

Here S_{abs} is the flux density after IGM absorption, and $S_{\text{ini}} = S_{\text{ext}}$ is the initial flux density in the rest frame including interstellar dust reddening given by Equation (2). In Figure 4, we show the D_A and D_B as a function of redshift. After obtaining S_{abs} , we get the S_{model} in Equation (1) for generating mock flux data.

We now estimate the flux error measured by the CSS-OS. For a space telescope, the signal to noise ratio (SNR) can be evaluated by (Ubeda et al. 2011)

$$\text{SNR} = \frac{C_{\text{st}} t}{\sqrt{C_{\text{st}} t + N_{\text{pix}}(B_{\text{sky}} + B_{\text{det}}) t + N_{\text{pix}} N_{\text{read}} R_n^2}}, \quad (4)$$

where t is the exposure time, N_{pix} is the number of detector pixels covered by an object for the CSS-OS, which can be derived from the values given by the COSMOS catalog, N_{read} is the number of detector readouts, B_{det} is the detector dark current, and R_n is the read noise. In the CSS-OS, we set $t = 300$ s, $N_{\text{read}} = 2$,

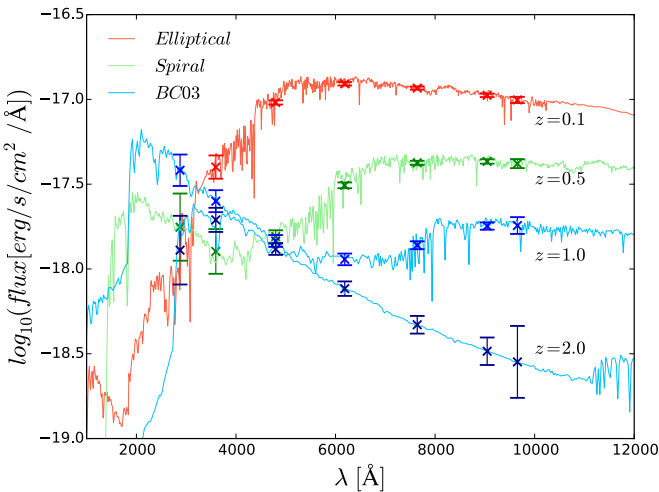


FIG. 5.— Examples of mock flux data of four galaxies for the seven bands of the CSS-OS at $z = 0.1, 0.5, 1.0$, and 2.0 . The curves denote the mock observed SED, and the crosses with error bars are the mock flux data. A random error that follows a Gaussian distribution function with $\sigma = \sigma_F$ is added to each mock flux data.

$B_{\text{det}} = 0.02 \text{ e}^-/\text{s}/\text{pixel}$, and $R_n = 5 \text{ e}^-/\text{pixel}$. C_s is the count rate from the source in e^-/s , which can be calculated by

$$C_s = A_{\text{eff}} \int S_{\text{obs}}(\lambda) T(\lambda) \frac{\lambda}{hc} d\lambda, \quad (5)$$

where A_{eff} is the effective aperture area of the telescope that varies for different bands, and h and c are the Planck constant and speed of light, respectively. B_{sky} in Eq. (4) is the sky background in $\text{e}^-/\text{s}/\text{pixel}$, which is given by

$$B_{\text{sky}} = A_{\text{eff}} \int I_{\text{sky}}(\lambda) l_p^2 T(\lambda) \frac{\lambda}{hc} d\lambda, \quad (6)$$

where I_{sky} is the surface brightness of the sky background in $\text{erg s}^{-1} \text{cm}^{-2} \text{\AA}^{-1} \text{arcsec}^{-2}$, and l_p is the detector pixel scale. B_{sky} depends on many components, such as the zodiacal light, earthshine, phase of moon, etc. Here we estimate B_{sky} based on the throughput of our filters and the measurements of the zodiacal light and earthshine for “average” sky background case given in Ubeda et al. (2011). We find that B_{sky} is $0.003, 0.020, 0.145, 0.193, 0.200, 0.124$ and $0.037 \text{ e}^-/\text{s}/\text{pixel}$ for NUV, u, g, r, i, z and y band, respectively.

We note that the SNR estimate given above is conservative, which gives $\text{SNR}=5$ for $g = 26$, and we will adopt it in the following discussion. For the optimistic case, we find that $\text{SNR} \simeq 8$ for $g = 26$.

The photometric error can be evaluated by the magnitude error given by the approximate relation $\sigma_{\text{ph}} \simeq 2.5 \log_{10} [1 + 1/\text{SNR}]$ (Bolzonella et al. 2000). We also add a systematic error $\sigma_{\text{sys}} = 0.02 \text{ mag}$ for all observational data, and the total magnitude error is then given

by $\sigma_m = \sqrt{\sigma_{\text{ph}}^2 + \sigma_{\text{sys}}^2}$. Then we can find the flux error σ_F for each band from σ_m via error propagation. In Figure 5, examples of mock flux data of four galaxies are shown at $z = 0.1, 0.5, 1.0$, and 2.0 . Finally, to each mock flux, a random error that follows a Gaussian probability distribution function (with $\sigma = \sigma_F$) is added.

3. PHOTO-Z CODE

In this section, we test three widely used photo- z template-fitting codes, i.e. LePhare³(Arnouts et al. 1999; Ilbert et al. 2006), EAZY⁴(Brammer et al. 2008), and Hyperz⁵(Bolzonella et al. 2000). Using the galaxy catalog and the mock flux data described in the last section, we fit the photometric redshift with these three codes, respectively. In order to compare the fitting results, we use the same SED templates provided by LePhare for all these three codes. In these codes, the photometric redshift is derived by the least-square method, which minimizes the following chi-square:

$$\chi^2 = \sum_i^N \left(\frac{F_i^{\text{obs}} - F_i^{\text{th}}}{\sigma_i^{\text{obs}}} \right)^2, \quad (7)$$

where N is the number of bands, F_i^{obs} and σ_i^{obs} are the observed flux and error for band i , respectively, which are derived from the mock flux data in the last section. F_i^{th} is the predicted flux by photo- z fitting code.

In Figure 6, we show z_{input} vs. z_{output} for the three photo- z codes. Here $\Delta z = z_{\text{output}} - z_{\text{input}}$, where z_{input} and z_{output} are input and output redshifts, respectively, σ_z is the total deviation of the photo- z fitting. Here we take the normalized median absolute deviation (NMAD) in the calculation, and it is given by

$$\sigma_{\text{NMAD}} = 1.48 \times \text{median} \left(\left| \frac{\Delta z - \text{median}(\Delta z)}{1 + z_{\text{input}}} \right| \right). \quad (8)$$

The advantage of this deviation is that it can naturally suppress the weighting of catastrophic redshift identifications, which is defined as $|\Delta z|/(1 + z_{\text{input}}) > 0.15$ here, and give a proper estimation of the total photo- z accuracy. We find that $\sigma_z = \sigma_{\text{NMAD}} = 0.023$ and the catastrophic redshift fraction $f_c = 7.05\%$ for LePhare, which is the most accurate photo- z result (for reference, $\sigma_z = 0.018$ and $f_c = 4.76\%$ for the optimistic case). The results of Hyperz are $\sigma_z = 0.028$ and $f_c = 4.70\%$, and they are greater than the results of LePhare. EAZY gives $\sigma_z = 0.031$ and $f_c = 8.66\%$, which are higher than the results of both LePhare and Hyperz. Hereafter, we would use the LePhare code to fit photo- z and perform the filter calibration.

In the photo- z fitting process discussed above, we discard data points in bands where they are too low to be detected above 3σ sensitivity limits.. Obviously, this can lead to information loss for the bands with low detection efficiency, especially for the NUV, u, z and y bands as shown in the right panel of Figure 1. However, the data in these four bands are quite valuable for distinguishing the Lyman and Balmer break features of galaxy SED, and can suppress the fraction of catastrophic redshift.

In order to exploit information in upper-limits, we make use of the following total χ^2 in the estimation, which can be expressed as

$$\chi_{\text{tot}}^2 = \chi_N^2 + \sum_j^M w_j, \quad (9)$$

³ <http://www.cfht.hawaii.edu/~arnouts/LEPHARE/lephare.html>

⁴ <http://www.astro.yale.edu/eazy/>

⁵ <http://webast.ast.obs-mip.fr/hyperz/>

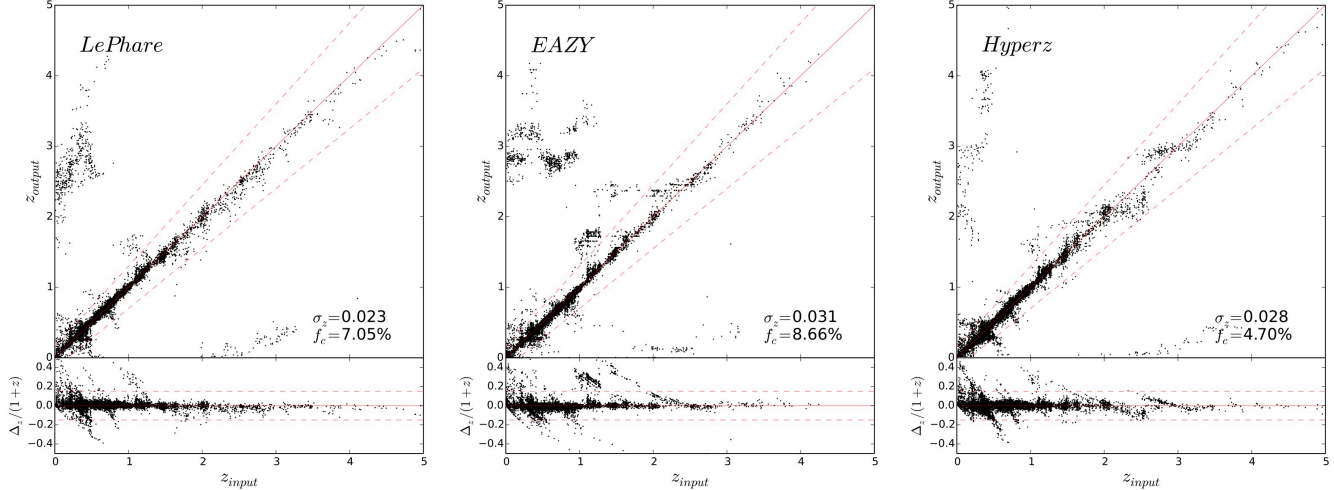


FIG. 6.— The photometric redshift fitted by the LePhare, EAZY and Hyperz codes. We find that LePhare gives $\sigma_z = 0.023$ and $f_c = 7.05\%$, which is the most accurate photo- z result. For comparison, EAZY and Hyperz give $\sigma_z = 0.031$ and $f_c = 8.66\%$, and $\sigma_z = 0.028$ and $f_c = 4.70\%$, respectively. The red dashed lines indicate the bounds of the catastrophic redshift identification, which is defined as $|\Delta z|/(1+z_{\text{input}}) > 0.15$.

where χ^2_N is for the data with $\text{SNR} \geq 3$ as shown in Eq. (7), M is the number of the bands with upper-limits, and $w_j = -2 \log P_j$. Here P_j is given by

$$P_j = \frac{1}{\sqrt{2\pi}\sigma_j} \int_{F_l}^{F_u} \exp \left[-\frac{(f - F_j^{\text{th}})^2}{2\sigma_j^2} \right] df, \quad (10)$$

where f is the flux variable, F_j^{th} is the flux calculated by the photo- z code for band j , σ_j is the flux error of band j , F_l and F_u are the flux lower and upper limits, and we take $F_l = 0$ and $F_u = 3\sigma_j$. Such a χ^2 enables a maximum-likelihood estimation of photo- z (Isobe et al. 1986; Lyu et al. 2016). As we discuss below, this method can naturally include the information in upper-limits, and efficiently suppress the catastrophic redshift fraction.

We modify the LePhare code by replacing Eq. (7) with Eq. (9). The results are presented in Figure 7. We find that $\sigma_z = 0.023$ is the same as that without including the upper limits, since our σ_z is insensitive to the catastrophic redshift. On the other hand, the current catastrophic redshift fraction $f_c = 2.14\%$, which is significantly improved compared to $f_c = 7.05\%$ given by the case without including the upper limits. For the optimistic case, we find that $\sigma_z = 0.018$ and $f_c = 0.97\%$ when including the upper-limit information. By comparing Figure 7 and the left panel of Figure 6, we can see that the number of the poorly fitted dots around $z_{\text{input}} = 0.3$ and 3 , which are caused by the misidentification of Lyman and Balmer breaks in SEDs, is remarkably suppressed. Hence, our method can properly take into account of the information in upper-limits, significantly reduce the catastrophic redshift fraction, and improve the accuracy of photo- z calibration. We will adopt this method in our following discussion about filter calibration.

4. FILTER CALIBRATION

After obtaining mock flux data and errors, we use the modified LePhare code to perform filter calibration. We first explore the effect of each filter passband on photo- z accuracy by removing it. We then try to find the

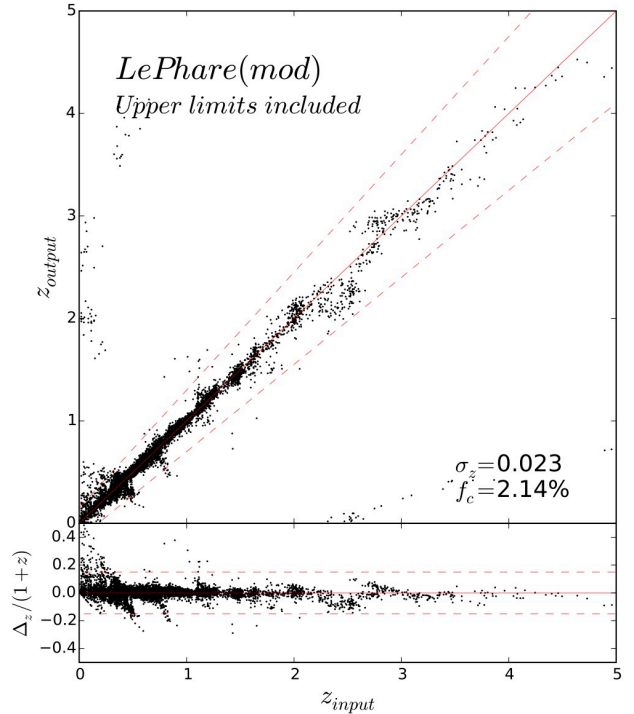


FIG. 7.— The photo- z fitting results including the information in upper-limits using Eq. (9). Although σ_z is similar, the catastrophic redshift fraction $f_c = 2.14\%$, which is significantly improved compared to $f_c = 7.05\%$ without considering the information of upper limits as shown in the left panel of Figure 6.

best filter parameters, such as the wavelength position, the wavelength width and the slope of the transmission curve, for optimizing photo- z fitting.

4.1. Dependency of photo- z accuracy on each band

In Figure 8, we show the result of photo- z fitting for the seven filter bands in our survey with removing the NUV , r and y bands, and including additional J and H bands at NIR, respectively. The σ_z and f_c results of removing each single band are shown in Table 2. We study two cases of the filters with real and 100% detec-

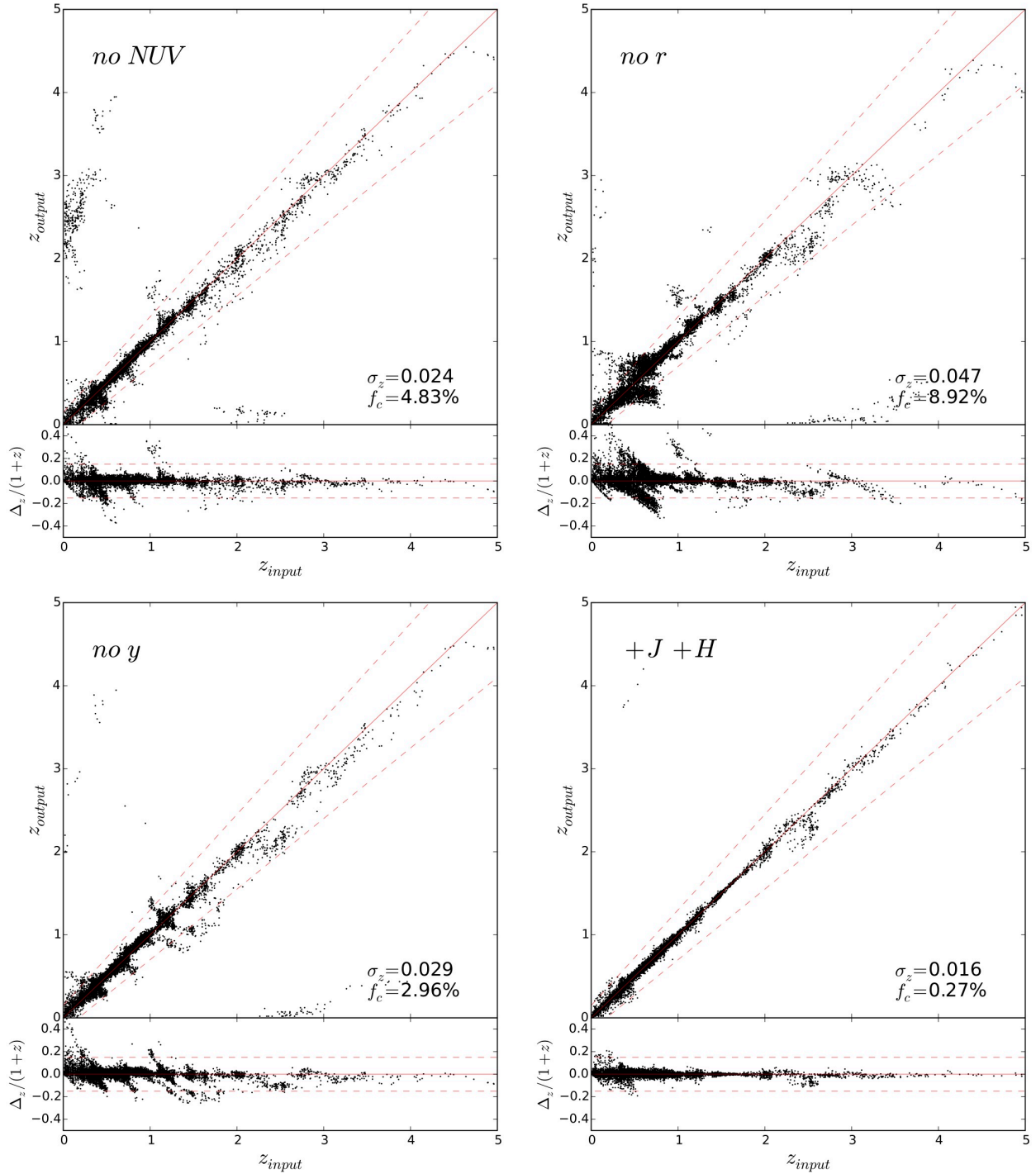


FIG. 8.— The photo- z fitting results for the seven bands without NUV , r and y , and with $J + H$ bands, respectively. We find that the NUV , u , g , r , and i bands have large effects on the photo- z results, and the missing of these bands will significantly suppress the photo- z accuracy. On the other hand, the z and y bands don't affect the results as much as the other five bands in our fittings. The J and H bands at longer wavelengths can improve the fitting results, especially for the objects at $z \gtrsim 4$. However, since there are not many objects at $z > 4$ in our survey, these two bands don't change the overall fitting results much. Note that the results of “no NUV ”, “no r ”, and “no y ” are assuming the real detector efficiency, and it is 100% efficiency for the result of the “ $+J + H$ ” case.

TABLE 2
THE REDSHIFT FITTING VARIANCE σ_z AND CATASTROPHIC REDSHIFT FRACTION f_c FOR DIFFERENT FILTER SETS.

Filter set	real det. eff.		100% det. eff.	
	σ_z	$f_c(\%)$	σ_z	$f_c(\%)$
All	0.023	2.14	0.019	0.81
-NUV	0.024	4.83	0.019	2.24
-u	0.027	4.87	0.022	2.50
-g	0.045	7.91	0.033	4.32
-r	0.047	8.92	0.030	2.24
-i	0.039	4.88	0.029	2.04
-z	0.032	2.76	0.023	1.20
-y	0.029	2.96	0.024	1.23
+J	-	-	0.016	0.48
+J + H	-	-	0.016	0.27

tor efficiencies as shown in the right and left panels of Figure 1, respectively. Since the transmission efficiencies are higher for all seven bands, we find that the results of 100% detector efficiency are generally better than that of the real efficiency case.

When removing the *NUV* band, as expected, we find that $\sigma_z = 0.024$ and $f_c = 4.83\%$, which are higher than $\sigma_z = 0.023$ and $f_c = 2.14\%$ in the case that it is included. The catastrophic redshift fraction f_c increases significantly, since we can see that there are many poorly fitted objects around $z = 0.1$ and 2 in the top-left panel of Figure 8 compared to Figure 7. The effect of *u* band is similar to that of the *NUV* band, but has slightly larger impact on the fitting results. This indicates that the *NUV* and *u* band is important to pin down the number of catastrophic redshifts.

As shown in Table 2, the *g*, *r* and *i* bands can significantly affect the photo-*z* fitting results, and they even have greater effect than the *NUV* and *u* bands, especially for the *g* and *r* band. We have $\sigma_z = 0.047$ and $f_c \sim 9\%$ if removing the *r* band, which can decrease the photo-*z* fitting accuracy dramatically. By checking the z_{input} vs. z_{output} results (e.g. see the top-right panel of Figure 8 for removing the *r* band), we find that the *g*, *r* and *i* bands mainly affect the fittings at $z = 0 \sim 0.5$, $0.3 \sim 0.8$, and $0.7 \sim 1.3$, respectively. The redshift dots in these ranges do not follow tightly the line $z_{\text{output}} = z_{\text{input}}$, but spread around it.

On the other hand, the *z* and *y* bands has smaller effects on the catastrophic redshift than the other five bands. Removing the *z* or *y* band can suppress the fitting accuracy at $z \sim 1.5$ and $z \gtrsim 3$ (see the bottom-left panel of Figure 8 for the effect of removing the *y* band). However, they don't have large effects on the fitting results, since the number of objects in this redshift range is relatively small given by our redshift distribution as shown in Figure 2.

In addition to these seven bands, we also investigate the photo-*z* calibration with other NIR bands, such as the *J* and *H* bands similar to the Euclid telescope (Lau-reijs et al. 2011). We set $\lambda_{lb} = 1050$ nm, $\lambda_{rb} = 1400$ nm, $\lambda_{lt} = 1100$ nm, and $\lambda_{rt} = 1350$ nm for the *J* band, and $\lambda_{lb} = 1350$ nm, $\lambda_{rb} = 2000$ nm, $\lambda_{lt} = 1400$ nm, and $\lambda_{rt} = 1950$ nm for the *H* band. The top transmission of these two bands is assumed to be 92%, which is the same as that of the *i*, *z*, and *y* bands. Then we perform photo-*z* fitting using these two bands for the 100% de-

tector efficiency case. As we can see in Table 2 and the bottom-right panel of Figure 8, the photo-*z* accuracy is improved by including these two bands. After comparing the plots of z_{input} vs. z_{output} , we find that these two bands mainly can enhance the fitting accuracy at $z \sim 2$ and $z \gtrsim 4$, since they are located at longer wavelengths (Liu et al. 2017). Because there are not many objects in this redshift range for our survey, the overall improvement is limited. These two bands are more important in photo-*z* fitting for the surveys with higher magnitude limits which can observe more faint high-*z* objects.

4.2. Dependency of photo-*z* accuracy on filter parameters

The definition parameters of the filters of photometric surveys also can affect the accuracy of photo-*z* calibration. Here we focus on three main parameters of filter transmission curves, i.e. the position of the central wavelength for band x λ_c^x , the wavelength coverage or width $\Delta\lambda^x$, and the slope of transmission curve s^x .

In the top panel of Figure 9, we show the σ_z and f_c as a function of λ_c . Here we use a shift scale in Å to denote the positions of bands relative to the original positions given in Figure 1 and Table 1, and the shift range is from -700 to $+700$ Å. In order to show the effect of each band clearly, we shift one band at a time when the other six bands are fixed at their original positions. We explore two cases of both the real and 100% detector efficiencies. We find that the variation of the fitting results for the two cases are generally similar. The result for the original position case, where the shift scale is equal to 0, is at the valley bottom of the curves. It indicates that the original positions of the seven filters are proper for photo-*z* calibration. At the edges of the shift range, σ_z and f_c of most bands increase significantly. This is apparently true, since the shifted band will be overlapped with an adjacent band if the shift range is too large. We also find that the values of σ_z and f_c tend to be smaller when the *y* band shifts to right (longer wavelengths) for the 100% efficiency case. This is because that the *y* band will act as an additional *J* or *H* band in this case, since the original *y* band is overlapped with the *z* band in our survey. On the other hand, this is not true for the real efficiency case, because the real detector efficiency can severely suppress the transmission of the *y* band when it shifts to longer wavelengths.

In the middle panel of Figure 9, the σ_z and f_c as a function of band width are shown. A width factor a is adopted to adjust the original band width $\Delta\lambda_{\text{ori}}$, and the tested band width is given by $\Delta\lambda = a \Delta\lambda_{\text{ori}}$. The range of a is from 0.5 to 1.5. In principle, the band width cannot be too wide or too narrow, since both cases can lead to the information loss of the SED features. However, wider band width can increase the number of received photons and enhance the strength of signal. Therefore, as can be seen in Figure 9, narrowing the band width can result in larger effect of increasing σ_z and f_c than that of broadening the band width. The σ_z and f_c of the *NUV* and *u* bands even become smaller by increasing band width (especially for the 100% efficiency case). Our original band widths, where the width factor $a = 1$, are around the minimum σ_z and f_c , and the band width for each filter doesn't affect the photo-*z* results significantly

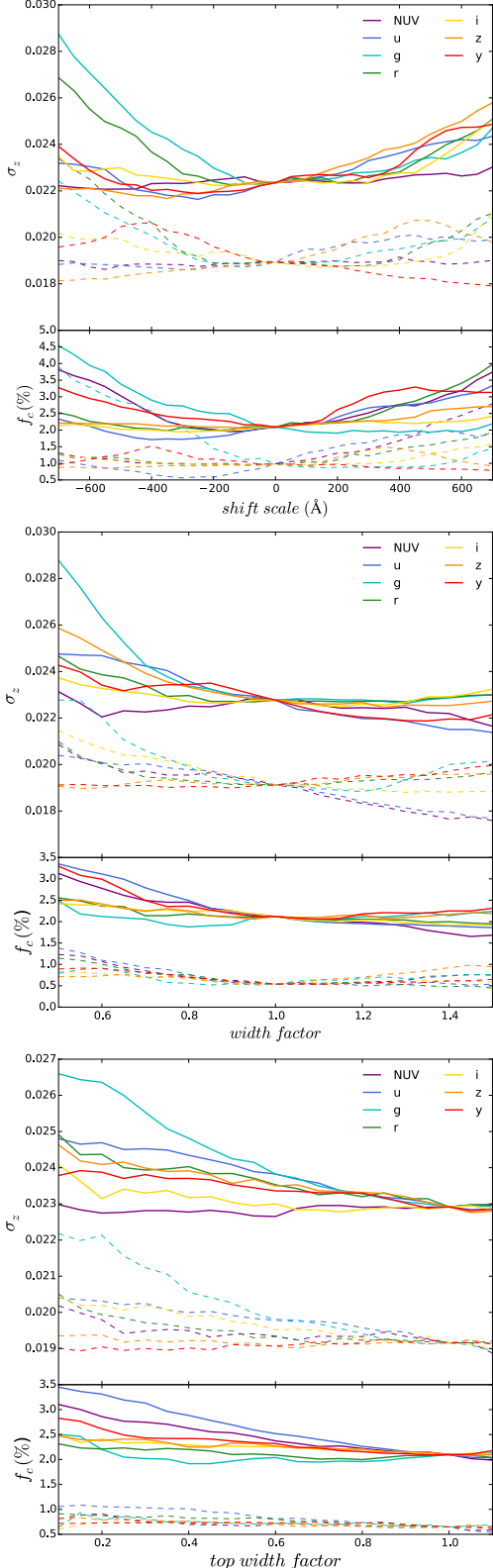


FIG. 9.— The σ_z and f_c as functions of the three filter parameters λ_c^x , $\Delta\lambda_c^x$, and s^x . Here we show the results as functions of the shift scale of λ_c^x in Å in the top panel, the width factor a multiplied on $\Delta\lambda_c^x$ in the middle panel, and the factor b multiplied on the top width of transmission curve in the bottom panel. The solid and dashed curves are for the real and 100% detector efficiencies, respectively.

if $0.8 \lesssim a \lesssim 1.2$.

In the bottom panel of Figure 9, the results of varying the slope of the transmission curve are shown. To change the slope, we make use of a factor b of the top width of the intrinsic transmission curve shown in the left panel of Figure 1, while fixing the bottom width of the curve. Then the top width $\Delta\lambda_t = b \Delta\lambda_t^{\text{ori}}$, where $\Delta\lambda_t^{\text{ori}}$ is the original top width. The b range we explore is from 0.1 to 1.1, and the top width will be larger than the bottom width if $b \gtrsim 1.1$ for all of the bands. We find that the original slopes for both real and 100% detector efficiency cases are at the minimum values of σ_z and f_c . For shallower or steeper slopes where $0.9 \lesssim b < 1.1$, the changes of σ_z and f_c can be neglected. For $b < 0.6$, the variances of σ_z and f_c become considerable.

However, we need to note that, we vary the filter parameters for one band at a time when fixing the other six bands as the original definition. This process can show the effect of photo- z fitting for each band clearly, but strictly speaking, it does not necessarily find the best filter parameters that can maximize the photo- z accuracy. In order to obtain the global minimum σ_z and f_c , and find the best parameters, we need to vary the filter parameters for all bands simultaneously. In this case, the computation complexity is proportional to M^N , where M is the number of values for one filter parameter, and N is the number of filters. This is quite complicated and time-consuming given by the current values of $M \sim \mathcal{O}(100)$ and $N = 7$. We would study it particularly in the future work.

5. SUMMARY

In this work, we study the dependency of photo- z fitting accuracy on the filter definition of photometric surveys. As an example, we examine the performance of the CSS-OS. It has seven filter passbands that cover a large wavelength range from the NUV to NIR bands. We adopt the COSMOS galaxy catalog with the similar magnitude limits as our survey. This catalog can represent our survey as real as possible, and it can provide similar observed galaxy redshift distribution, magnitude distribution, and galaxy types. Then we select galaxies with high data quality from this catalog, and use this selected sample in the photo- z fitting.

Then we calculate the mock observed flux and error for each band. We make use of thirty-one SED templates for elliptical, spiral, and young blue star forming galaxies, and extend their wavelength coverages from ~ 900 Å to ~ 90 Å using the BC03 method, since we have large wavelength coverage. We also consider the dust extinction effect from both interstellar dust of galaxy and the absorptions of the IGM, when estimating the mock flux data. The flux error is evaluated by considering several factors, such as the instrumental parameters, sky background, and systematic errors.

We compare three different photo- z SED template fitting codes: LePhare, EAZY, and Hyperz, and find that LePhare gives the best results for our survey. Furthermore, we improve the LePhare code by including upper-limits in the photo- z fitting. We show that this can remarkably suppress the catastrophic redshift fraction and improve the photo- z accuracy. By applying this method, in the conservative case, we find that $\sigma_z = 0.023$ and $f_c = 2.14\%$ for the CSS-OS.

Next, we explore the effect of photo- z fitting accuracy for each band. By removing one band at a time, we perform the photo- z fitting process, and calculate σ_z and f_c . We find that the g , r , and i bands have the largest impact on both σ_z and f_c , and the NUV and u bands can affect f_c significantly. On the other hand, the z and y bands have relatively smaller effect on f_c . Besides the seven bands in our survey, we also study other NIR bands at longer wavelengths, i.e. the J and H bands. We find that these two bands can improve the fitting accuracy for the objects at $z \gtrsim 4$. However, they don't have large effect for the overall fitting results, since the number of objects at $z > 4$ is small in our survey. But they should be more important for the surveys with higher magnitude limits, which can observe more faint high- z objects.

Finally, we investigate the dependency of photo- z accuracy on the parameters of filter transmission curve, such as the position of central wavelength for each band, the band width, and the slope of transmission curve. We

find that the position of each band has the largest effect on the photo- z fitting result, and the current design of the three filter parameters in our survey is proper and optimal.

YC and YG thank Yingjie Peng for helpful discussion. YG acknowledges the support of Bairen program from the National Astronomical Observatories, Chinese Academy of Sciences. YG and XLC acknowledge the support of NSFC-11633004. CKX acknowledges the support of NSFC-11643003. XLC acknowledges the support of the MoST 863 program grant 2012AA121701, the CAS grant QYZDJ-SSW-SLH017, and the NSFC through grant No. 11373030. DZL acknowledges the support of NSFC-11333001 and 11173001. YQX acknowledges the support of NSFC-11473026 and 11421303. LC, XF, XZ, SW, and HZ were partially supported by the China Manned Space Program.

REFERENCES

LSST Science Collaborations: Abell, P. A., Allison, J., Anderson, S. F., et al. 2009, arXiv:0912.0201

Allen, C. W. 1976, *Astrophysical Quantities*, University of London, The Athlone Press, 264

Arnouts, S., Cristiani, S., Moscardini, L., et al. 1999, MNRAS, 310, 540

Benitez, N. 2000, ApJ, 536, 571-583

Bolzonella, M., Miralles, J. M., & Pello, R. 2000, A&A, 363, 476

Bouchet, P., Lequeux, J., Maurice, E., Prevot, L., & Prevot-Burnichon, M.L. 1985, A&A, 149, 330

Brammer, G. B., van Dokkum, P. G., & Coppi, P. 2008, ApJ, 686, 1503-1513

Bruzual, G., & Charlot, S. 2003, MNRAS, 344, 1000

Calzetti, D., Kinney, A. L., & Storchi-Bergmann, T. 1994, ApJ, 429, 582

Calzetti, D., Armus, L., Bohlin, R.C., et al. 2000, ApJ, 533, 682

Collister, A. A. & Lahav, O. 2004, PASP, 116, 345

Feldmann, R., Carollo, C. M., Porciani, C., et al. 2006, MNRAS, 372, 565-577

Firth, A. E., Lahav, O., & Somerville, R. S. 2003, MNRAS, 339, 1195

Fitzpatrick, E.L., 1986, AJ, 92, 1068

Holwerda, B. W., Keel, W. C., Kenworthy, M. A., & Mack, K. J., 2015, MNRAS, 451, 2390

Ilbert, O., Arnouts, S., McCracken, H. J., et al. 2006, A&A, 457, 841

Ilbert, O., Capak, P., Salvato, M., et al. 2009, ApJ, 690, 1236-1249

Isobe, T., Feigelson, E. D., & Nelson, P. I. 1986, ApJ, 306, 490-507

Laigle, C., McCracken, H. J., Ilbert, O., et al. 2016, ApJS, 224, 24

Laureijs, R., Amiaux, J., Arduini, S., et al. 2011, arXiv:1110.3193

Liu, D., Yang, J., Yuan, S., et al. 2017, ApJ, 153, 53

Lyu, J., Rieke, G. H., & Alberts, S. 2016, ApJ, 816, 85

Madau, P. 1995, ApJ, 441, 18

Polletta, M., et al. 2007, ApJ, 663, 81

Prevot, M. L., Lequeux, J., Maurice, E., & Rocca-Volmerange, B. 1984, A&A, 132, 389

Reddy, N. A., Kriek, M., Shapley, A. E., et al. 2015, ApJ, 806, 259

Seaton, M. J. 1979, MNRAS, 187, 73

Ubeda, L., et al. 2011, ACS Instrument Handbook, Version 11.0 (Baltimore: STScI)

Zhan, H. 2011, Scientia Sinica Physica, Mechanica & Astronomica, 41, 1441